

Non-equilibrium in the solar neighbourhood using dynamical modelling with *Gaia* DR2

Rain Kipper¹,^{*} Peeter Tenjes,¹ Elmo Tempel¹ and Roberto de Propriis²

¹*Tartu Observatory, University of Tartu, Observatooriumi 1, 61602 Tõravere, Estonia*

²*Finnish Centre for Astronomy with ESO (FINCA), University of Turku, Vesilinnantie 5, FI-20014 Turku, Finland*

Accepted 2021 July 19. Received 2021 June 1; in original form 2020 December 4

ABSTRACT

Matter distribution models of the Milky Way galaxy are usually stationary, although there are known to be wave-like perturbations in the disc at ~ 10 per cent level of the total density. Modelling of the overall acceleration field by allowing non-equilibrium is a complicated task. We must learn to distinguish whether density enhancements are persistent or not by their nature. In this paper, we elaborate our orbital arc method to include the effects of massless perturbations and non-stationarities in the modelling. The method is tested by modelling of simulation data and shown to be valid. We apply the method to the *Gaia* Data Release 2 (DR2) data within a region of ~ 0.5 kpc from the Sun and confirm that acceleration field in the solar neighbourhood has a perturbed nature – the phase-space density along the orbits of stars grow in the order of $h \lesssim 5$ per cent per Myr due to non-stationarity. This result is a temporally local value and can be used only within the time frame of a few Myr. An attempt to pinpoint the origin of the perturbation shows that the stars having larger absolute angular momentum are the main carriers of the local perturbation. As they are faster than the average thin disc star, they are either originating further away and are close in their pericentre or they are perturbed locally by a fast comoving perturber, such as gas disc inhomogeneities.

Key words: Galaxy: fundamental parameters – Galaxy: kinematics and dynamics – Galaxy: structure.

1 INTRODUCTION

Although in general galaxies are not isolated in space and are thus dynamically interrelated, their mass distribution models are usually stationary (see e.g. a review by Rix & Bovy 2013) or related to some specific aspect of galaxy, e.g. phase-space spirals in Widmark et al. (2021). The stationarity assumption is a widely used approximation as the periods of stellar oscillations in a typical galaxy are less than a Gyr. Stationary models often allow us to describe the internal velocity distribution quite satisfactorily (Cappellari et al. 2013; Leung et al. 2018; Zhu et al. 2018).

Although stationary modelling can provide satisfactory results in modelling, there are slow changes in discs shaped by minor mergers (Abadi et al. 2003; Villalobos & Helmi 2008; Moster et al. 2010; Bird, Kazantzidis & Weinberg 2012). Stellar haloes may be formed as due to disruption of several tens of dwarf galaxies (Johnston et al. 2008), assembly of the dark halo from subhaloes created fluctuating overall potential influencing visible components of galaxies (Carlberg 2019; Vasiliev, Belokurov & Erkal 2021). In addition to these minor events in case of the Milky Way (MW) galaxy there have been in the past by at least one significant merger (Helmi et al. 2018). Although most of these ancient marks of the mergers are smoothed out by now, the traces remain still visible in action space.

Recent observations give a strong hint that there are time-dependent perturbations of the density in our Galaxy and conventional dynamics modelling need improving (Haines et al. 2019;

Salomon et al. 2020). Systematic vertical motions in the stellar disc and north–south asymmetry were found by Widrow et al. (2012), Williams et al. (2013), Carlin et al. (2013), and Yanny & Gardner (2013). *Gaia* satellite has also revealed a rather complex structure of the MW galaxy in 6D phase space. For example, Ramos, Antoja & Figueras (2018) found from *Gaia* Data Release 2 (DR2) data that the phases of stars are not well mixed for all orbits. Antoja et al. (2018), Kawata et al. (2018), and Trick, Coronado & Rix (2019) also found similar arcs and ridges.

Observations of systematic vertical motions imply that MW disc is undergoing compression and expansion perpendicular to the plane (Banik, Widrow & Dodelson 2017). These perturbations can be caused by the passages of globular clusters, dwarf galaxies, dark matter subhaloes, passing spiral arms, etc.

The main obstacle regarding the modelling of perturbed systems arises from collisionless Boltzmann equation:

$$\frac{\partial f}{\partial t} + \sum_{i=1}^3 \frac{\partial f}{\partial v_i} \frac{dv_i}{dt} + \frac{\partial f}{\partial x_i} \frac{dx_i}{dt} = 0. \quad (1)$$

Here f is the phase-space density and i indexes components of velocity and position vectors \mathbf{v} and \mathbf{x} . It contains one observable variable (phase-space density) and its spatial derivatives. But it also contains a time derivative, which is not directly observable, and accelerations (gravitational potential gradient components) that are also not observable. Hence there is only one equation and two unknowns, making the equation unsolvable. The presence of dark matter and too dim objects in mass distribution does not also allow the Poisson equation to constrain the acceleration field.

* E-mail: rain.kipper@ut.ee

Time derivatives indicate that it would be correct to handle the potential as a function of time $\Phi(\mathbf{x}, t)$ and it may change noticeably model results derived within a stationary model. It is also necessary to estimate how reasonable the assumption of a stationary potential is or within what time-scale one can handle integrals of motions to be constant for a particular stellar orbit. For example, by modelling the MW bar with *Gaia* DR2 data Kipper et al. (2020) estimated that due to torque from the central bar the angular momentum of the Sun L_z might change within one orbital period about 30 per cent. It indicates that in barred galaxies L_z is not as good integral of motion as one would like it to be. Conventional models should be handled as an approximation only. Slow changes of the angular momentum L_z and radial action J_R were derived from N -body simulations by Wozniak (2020), although they derived slower diffusion of these values.

Modelling of individual galaxies via N -body simulations (e.g. made to measure) is in some sense free of a stationarity assumption, but these models are rather time-consuming, and their spatial and mass resolution is yet moderate (Syer & Tremaine 1996; de Lorenzi et al. 2007; Long & Mao 2010; Zhu et al. 2014).

In our earlier paper (Kipper, Tempel & Tenjes 2019), we presented a method to calculate gravitational potential derivatives (accelerations) in sufficiently small regions of a galaxy if one knows phase-space coordinates of a large number of stars in these regions. In a later paper (Kipper et al. 2020), the method was applied for the MW galaxy in the solar neighbourhood (SN) using *Gaia* DR2 data. The model included a non-axisymmetric central bar but assumed stationarity. In this paper, we improve the method by allowing non-stationarity, i.e. that the phase density is a function of time. As the observational data we use *Gaia* DR2 phase-space coordinates.

It is not our aim here to describe the secular evolution of galaxies, although, in principle, it is not excluded. Although a perturbation can last for an extended period, we model only a short time interval. This interval is determined both by the size of the studied region and the average speed of stars in that region. Extrapolation of the derived results for longer time-scales than few Myr is not justified. To emphasize this short-timed characterization, we mainly use the word perturbation to describe the system's time evolution/non-stationarity. The selected small region of the MW is in the SN and used stars have all six phase-space coordinates from the *Gaia* DR2.

In Section 2, we characterize the advancements we did in modelling compared to Kipper et al. (2020) in more detail. Section 3 checks the validity of the improvements with mock data. Thereafter, in Section 4, we present what we learned about the SN using this approach. The paper ends with discussion (Section 5) and conclusions (Section 6).

2 ADVANCEMENTS OF THE METHOD

The improvements of the method presented by Kipper et al. (2020) are related to both dynamics and statistics. We describe them in subsequent sections. However, we provide a concise recap of the method we build our improvements.

The orbital arc method developed in Kipper et al. (2020) relies on seeking of consistency between assumptions and data. The data in our case is the distribution of stars in a specific region. First, we start selecting observed positions and velocities of a localized sample of stars and consider them as initial conditions for orbit calculations. We take the initial conditions, assume an acceleration with some free parameters and calculate small arcs of orbits for all the stars within the selected region. Coefficients in the acceleration field are found by demanding that the acceleration field in orbit calculations would distort the phase-space distribution of stars in the least way compared

to the phase-space distribution constructed from initial conditions (observed values). By distorting we mean a changing the phase space by repositioning a star infinitely many times along its orbital arc, or more precisely, we smooth the star over its short piece of orbit *uniformly in time*. This procedure assumes stationarity. If the system is stationary, then the smoothed distribution and the data distribution would match, i.e. the likelihood for the statistical inference found by evaluating initial conditions of the same stars with the distorted phase-space distribution would be maximal. The inference gives us the acceleration field that best matches the stationarity of the data distribution.

2.1 Improved description of kinematics

Modelling the distribution and kinematics of stars in SN, Bennett & Bovy (2018) found that on top of the smooth distribution there are also wavy motions with the amplitude of about 10 per cent. Hence, about 10 per cent of the stellar density in the SN has perturbed nature. If we intend to model the MW with an accuracy greater than this, we must find a way to cope with these perturbations. At first sight, the easiest way is to model the MW by using data that are distributed over a much larger area than the SN and average out these perturbations. The smoothed distribution can be modelled using tools designed to model stable and stationary systems. This would provide a global MW model, and on top of this model, a perturbation model can be constructed. A drawback of it is the necessity to have a large amount of data over a large region, and the unknown perturbations might be too large-scale to average out (e.g. the bar). Also, it hinders to find the details of the calculated acceleration field: recovered details cannot be finer than the scale that the data were averaged out. In case of some form of perturbations, such as bar, the system can be modelled in a rotating frame to avoid the perturbations and time dependence, but it introduces an additional free parameter.

This section will augment the orbital arc method (Kipper et al. 2019, 2020) to include the modelling of a region in the Galaxy being in a perturbed state. In this paper, we only aim to model perturbations that do not contain a significant amount of mass and are dominantly density perturbations leaving potential and acceleration field untouched. This approach is justified as the potential is essentially determined by a large amount of matter distributed over all galaxy, not locally.¹

The orbital probability density function (oPDF) formalism from Han et al. (2016) demonstrated that in a stationary galaxy the relation between a time interval (dt) and probability of finding a star in corresponding orbital segment (dP) is

$$dP \propto dt. \quad (2)$$

If we intend to model a galaxy in a perturbed state, this simple proportionality does not hold anymore and if we want to use this kind of relation, we should add a perturbation term in order to cope with it:

$$dP \propto [1 + h'(t)] dt. \quad (3)$$

Here, the $h'(t)$ term describes the perturbation of the dynamical state of a galaxy. Yet, adding a random term to equation (3) does not make it more correct or more apt to describe the underlying structure of a galaxy; so why would it work?

¹As $\nabla^2 \Phi = 4\pi G \rho$ density fluctuations determine only the second derivative of the potential fluctuations.

Let us imagine a galaxy consisting of only one densely populated orbit (i.e. a stellar-stream-like entity). We assume the stars are positioned along the orbit according to equation (2). Initial conditions and acceleration field fully determine orbit's shape. In case of orbital arc method, we may take any star from the orbit and infer the underlying acceleration field by matching proposed orbits with the rest of the stars in our hypothetical galaxy. As the orbit was populated with the assumption of stationarity, the matching required by the orbital arc method is expected to be perfect.

Let us keep this hypothetical galaxy, but let us populate the orbit according to a perturbed/non-stationary state: some parts of the orbit have an elevated number density of stars. Again, orbital arc calculations can reproduce the shape of the orbit similarly well as the neighbouring points have the same kinematics as the previous case. The only differences are different number densities along the orbit. Thus, the number density of stars along an orbit depends both on the unperturbed velocities along the orbit and on the perturbations. An illustration in Fig. 1 shows this concept visually.

The stellar part of a galaxy contains a multitude of orbits overlapped with each other. Even in case of summing over all the orbits in our selected region, the shapes of orbits give us the velocity gradients in the region – the orbit shapes determine dv/dx and due to fixed initial conditions df/dv is fully determined by acceleration field too. The non-stationarity does not influence the shapes of the orbits, but their population density or df/dx directly while not affecting velocity gradients. The orbital arc is built to minimize changes to phase-space density, hence also to keep their gradients unchanged. We conclude that the reconstruction of phase-space density has different basis when we consider the sources of non-stationarity (influences only df/dx) and gravitational potential (influences df/dv directly and df/dx indirectly). A test with a simulation shows that it is a viable approach.

A more formal way to introduce this extra term to the oPDF in equation (3) comes from the collisionless Boltzmann equation. We start from and follow the work of Han et al. (2016). The classical Boltzmann equation (1) written using the integrals of motion is

$$\frac{\partial f}{\partial t} + \sum_{k=1}^5 \frac{\partial(f\dot{Q}_k)}{\partial Q_k} + \frac{\partial(f\dot{\lambda})}{\partial \lambda} = 0. \quad (4)$$

Here, the Q_k characterizes integrals or constants of motion and λ is the affine parameter characterizing position on the orbit. The parameter λ need not to have a specific interpretation – it is necessary only that in order to determine uniquely position on the orbit, λ must be growing monotonically along the orbit.

The definition of integral of motion means $\dot{Q}_k = 0$ and thus equation (4) is simply

$$\frac{\partial f}{\partial t} + \frac{\partial(f\dot{\lambda})}{\partial \lambda} = 0. \quad (5)$$

The assumption $\partial f/\partial t = 0$ leads to stationarity, which is not our aim at present. The simplest assumption not leading to stationarity is that $\partial f/\partial t \equiv \text{const} = A$ (assumption of a constant is only our first attempt here). For example, this form can describe an approaching overdensity toward a studied region in rotation-dominated disc. Let us make this substitution and integrate equation (5) with respect to λ :

$$A\lambda + f\dot{\lambda} = B, \quad (6)$$

where B is the integration constant. Solving the latter for f gives

$$f = (B - A\lambda) \frac{dt}{d\lambda}. \quad (7)$$

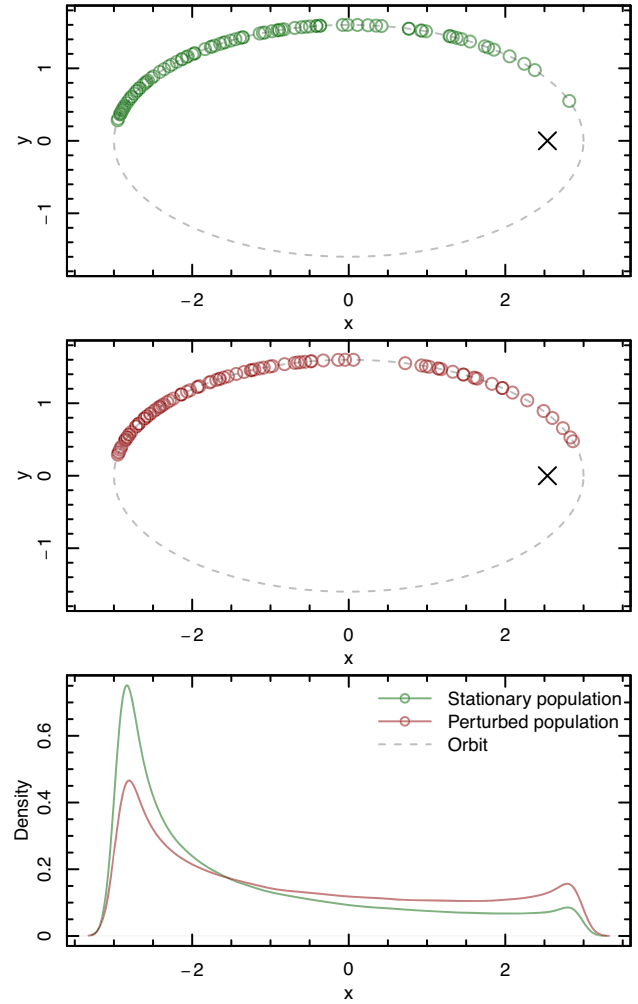


Figure 1. An illustration of the modification to the orbital arc method to model non-stationarities. The top panel shows the distribution of Keplerian orbit when the stars are populated in it according to orbital probability density function (oPDF) in equation (2). The black cross shows the focal point of the Keplerian orbit. The middle panel shows the distribution of stars positioned non-stationarily. The bottom panel shows the distributions of their x -coordinates, which do not match. The update to the method has the basis that the stellar initial conditions and acceleration provide identical orbit shape. However, non-stationarity affects phase space/population along the orbit without affecting velocity gradients.

The projection of phase-space density while fixing the integral of motions provides the probability density of finding a star along the orbit. Following the approach of Han et al. (2016) again and use equation (7), we find

$$\frac{dP}{d\lambda} |Q \propto f(Q, \lambda) = (B - A\lambda) \frac{dt}{d\lambda}. \quad (8)$$

In the left-hand side $|Q$ means for a given Q value. Multiplying by $d\lambda$ gives time span star spends in a segment of an orbit. When characterizing the position along the orbit with time² we may substitute $\lambda \rightarrow t$. Writing instead of $(-A/B) \rightarrow h$ we have a similar

²Other types of characterizations are possible, but in order to infer time evolution we selected time as the affine parameter.

expression to equation (3) with $h'(t) = ht$,

$$dP \propto (1 + ht) dt. \quad (9)$$

The practical application requires normalization of probability, hence we substituted the equality to proportionality. Equation (9) is derived for an orbit, i.e. $h = h|Q$. For applications we use an approach where the h depends only on one integral of motion: L_z . We have implicitly assumed that $t = 0$ is the time of observations.

To give an interpretation of h and the perturbedness, let us look at equation (7). Averaging equation (7) over the studied region, we have $\langle f \rangle = \langle B \rangle - \langle A \rangle = B$ as the time-dependence averages out. The time-dependence averages out since $t = 0$ is defined as the time of *Gaia* observations and deviations from it are symmetrical (on average star can move forward and backward the same amount before exiting the studied region) and cancel out. The term A was defined $A \equiv \dot{f}$, or $\langle A \rangle = \langle \dot{f} \rangle$. By normalizing the intercept term in equation (8) to one (required by normalization of probability) gives the interpretation of h to be $h \approx \langle \dot{f} \rangle / \langle f \rangle$ or the averaged relative perturbedness.

2.2 Improving statistical description

The *orbital arc* method is based on the assumption that the overall probability to find an observed point at position $p(\mathbf{q})d\mathbf{q}$ comes from the sum of i orbital densities; each described by probability to find a star in the orbital point $p_i[\mathbf{q}(\lambda)|\vartheta]$. We denote \mathbf{q} as an element of phase-space density, λ characterizes position along the orbit, and ϑ the acceleration field parameters. The underlying acceleration parameters are determined by maximizing the likelihood function with respect to the ϑ ,

$$\mathcal{L}'_g = \prod_{j \in S} p(\mathbf{q}_j) = \prod_{j \in S} Z^{-1} \sum_i p_i[\mathbf{q}|\vartheta] K_g(\mathbf{q}_j, \mathbf{q}). \quad (10)$$

Here the S is a set of stars in the region indexed by j , Z is the normalizing constant, and K_g is the kernel converting orbital arcs into a smooth probability distribution. More details are elaborated in Kipper et al. (2019).

The paper Kipper et al. (2020) had a drawback in statistical modelling that having a grid-based approximation of probability produced slightly distorted p values. In order to estimate and suppress it, we made multiple modelling and averaged the posterior distributions. We improve upon this by making multiple grids and p estimations, and each likelihood evaluation we average the likelihoods, i.e.

$$\mathcal{L} = \sum_{g=1}^G \mathcal{L}'_g. \quad (11)$$

Here \mathcal{L}'_g is a likelihood function defined by equation (10) but implemented with different grids in kernel K . The g indexes the likelihoods, and G is the number of grids averaged per likelihood evaluation. A more thorough description is provided in Kipper et al. (2021) in the context of modelling galaxy evolution.

The second improvement comes from the necessity of independence that the likelihood evaluation point cannot be included in the calculation of p . This is reached by requiring

$$i \neq j \quad (12)$$

in the summing over i in equation (10). In case the number of stars/point approaches infinity, this does not produce any practical bias, but in the case where the number of stars is lower, it might. A test on *Gaia* data showed that this effect is detectable and significant when the modelling is done with a fine grid.

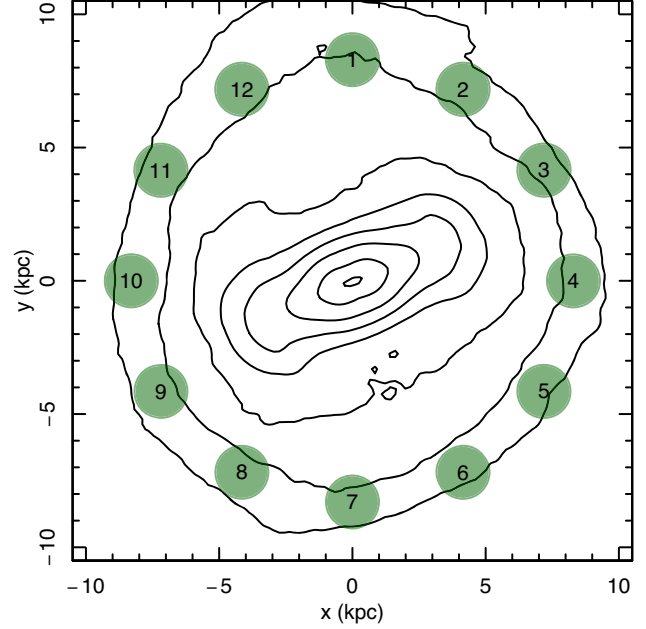


Figure 2. Sizes and positions of selected regions (green circles) for a simulated galaxy from Garbari et al. (2011) together with isodensity contours.

In the next section, we make a set of tests on a simulation. These tests showed that these modifications produced unbiased estimator for the acceleration field parameters.

3 VALIDATING THE IMPROVED METHOD ON A SIMULATION

Applying the method on a mock or a simulation gives us a possibility to test that the underlying method and its implementation are robust and correct. For the testing, we chose the simulation of an MW-like galaxy from Garbari, Read & Lake (2011). The aim is to test the assumption of non-stationarity and modifications made to improve its statistical implementation.

3.1 The mock data

We selected 12 small spheroidal regions to model: all of them at the distance of 8 kpc from the galactic centre. Here and onward we denote the regions as solar region (SR). This designation is usually used with the corresponding number of a region. In Fig. 2 positions of these regions together with isodensity contours of the simulated galaxy are shown. SRs have half-height of 0.35 and radius of 1.0 kpc. SRs are larger to compensate lower number density of stars in these regions, which otherwise would reduce the precision of modelling.

We calculated the pattern speeds for $R = 1.5\text{--}4.5$ kpc of the simulated galaxy by solving one of the intermediate results in Tremaine–Weinberg method derivation (Tremaine & Weinberg 1984):

$$\frac{\partial}{\partial x}(\Sigma v_x) + \frac{\partial}{\partial y}(\Sigma v_y) + \Omega_p y \frac{\partial \Sigma}{\partial x} - \Omega_p x \frac{\partial \Sigma}{\partial y} = 0. \quad (13)$$

Here, Σ is the surface density, x, y are Cartesian coordinates, and Ω_p is the pattern speed. Pattern speed in this bar region is rather constant at the value of $\Omega_p = 37.0^{+6.0}_{-5.4}$ km s⁻¹ kpc⁻¹. The uncertainty of 20 per cent is expected for the Tremaine–Weinberg method due to fluctuating nature (Hilmi et al. 2020).

3.2 Data sampling and systematic uncertainties

3.2.1 Sampling noise

For the method testing, the mock data should mimic the subsequent application as adequately as possible. The main differences with observations are that mock data are not limited by object brightnesses, the data have no uncertainties, they have perfect selection function, and have significantly smaller number density of stars. The brightness limit aspect was tested in Kipper et al. (2020) and is not covered here. The observational uncertainties are minimal as we constructed the observational data set using a very close set of stars (maximum distance is about half of a kiloparsec – kpc).

Thus, we test here only the sensitivity of the modelling due to the smaller number of stars compared to the observational application sample. This is essential as the model's accuracy is limited with the number of stars to construct the probability density function (PDF) in equation (10). An average SR contain about 60 000 stars. This is significantly less than the observational sample of 400 000 stars. We point out that we chose the larger region in simulation than in observational application to elevate the number of stars to be more comparable. To test how sensitive the method is to reducing the size of the sample, we modelled 10 subsamples of the SR1, each having 25 per cent less stars than the parent sample. The test results are in Fig. 3. It is seen a significant change of calculated a_R values for different subsamples. One notice also that all of them differ within uncertainties from the actual value. As all other possible causes have been checked and have smaller influence, we conclude that the reason is sampling. This is confirmed also by looking at the top panel of Fig. 13 where we can see significant high-frequency noise in acceleration, being also a side effect of sampling. In real observations the number density of stars is about an order of magnitude larger and one may expect the sampling effects to be significantly smaller. In any case, we cannot leave this discrepancy unattended and consider these differences as the cause of systematic uncertainty described in the next section.

3.2.2 Systematic uncertainties

In the previous section, we concluded that sampling could cause an offset between actual values and the modelled ones. To cover the possible offset, we describe it as systematic uncertainties (see Fig. 3).

Let us consider an abstract one-dimensional statistical inference problem modelled with the Markov chain Monte Carlo (MCMC) approach (Feroz & Hobson 2008; Feroz, Hobson & Bridges 2009; Feroz et al. 2019) similar to the MULTINEST we use in this paper. Let us have a point x and its proposed change to $x + \Delta x$. The change is accepted in Monte Carlo based on the log likelihood differences of these points,

$$\Delta \log \mathcal{L} = -\frac{1}{2} \frac{x^2}{\sigma_{\text{stat}}^2} + \frac{1}{2} \frac{(x + \Delta x)^2}{\sigma_{\text{stat}}^2} = \frac{1}{2} \frac{x \Delta x + \Delta x^2}{\sigma_{\text{stat}}^2}. \quad (14)$$

We assumed a normal distribution with a standard deviation of σ_{stat} here as most uncertainties in our preliminary modellings suggested it to be a valid approximation. If there is also a systematic component in uncertainties, the real likelihood difference should be

$$\Delta \log \mathcal{L}' = \frac{1}{2} \frac{x \Delta x + \Delta x^2}{\sigma_{\text{stat}}^2 + \sigma_{\text{sys}}^2}, \quad (15)$$

where also a systematic uncertainty of the modelling σ_{sys} is added. We may write

$$\Delta \log \mathcal{L}' = C \Delta \log \mathcal{L}, \quad (16)$$

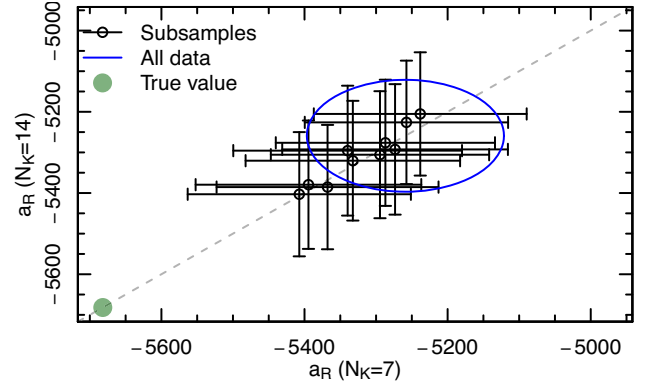


Figure 3. The sensitivity of the recovered acceleration to the sampling. 10 subsamples of SR1 each containing 75 per cent of the total sample are modelled and calculated acceleration values are presented with black colour. The blue circle shows the modelling results of the total sample and the green point the actual values from the gravitational potential. The x -axis is the recovered acceleration with coarser kernel function K_g having N_k^2 histogram bins. In the y -axis is the finer grid results. As either the uncertainty or error do not depend on the gridding, we conclude that the grid K details do not influence modelled results.

where C is the correction to include systematic uncertainty with the value

$$C = \frac{\sigma_{\text{stat}}^2}{\sigma_{\text{stat}}^2 + \sigma_{\text{sys}}^2} = \left(1 + \frac{\sigma_{\text{sys}}^2}{\sigma_{\text{stat}}^2}\right)^{-1}. \quad (17)$$

The advantage of including the systematic uncertainties in likelihood calculations is the ability to model all systematic uncertainties simultaneously and to preserve more accurate posterior distribution than adding systematic component.

Numerical values of C are calculated based on comparing modelling results and corresponding actual values (see Section 3.6.1).

3.3 Selection of acceleration field

To apply the method to the data, we must first assume a sufficiently flexible form of the acceleration field. As the sizes of the studied regions are small (their radii are about 1 kpc) the acceleration field can be described in a very concise way. We chose a Taylor-expansion-like forms:³ average components of the field with added correction terms in directions where acceleration components change significantly:

$$a_R = A_R + A_{R,R} \Delta R, \quad (18)$$

$$a_\theta = A_\theta, \quad (19)$$

$$a_z = A_z + A_{z,z} z. \quad (20)$$

Here we used usual cylindrical coordinates,

$$\Delta R = R - R_{\text{cnt}}, \quad (21)$$

and R_{cnt} corresponds to the centres of regions. We have denoted (a_R, a_θ, a_z) as the acceleration vector components. Capital letters A_R, A_θ, A_z are average acceleration components within a region (zero terms

³As most functions can be expanded to the Taylor series, comparison with global MW models can be done simply by expanding the global MW acceleration field into a Taylor series around the SN and by comparing thereafter expansion coefficients with our fitted values.

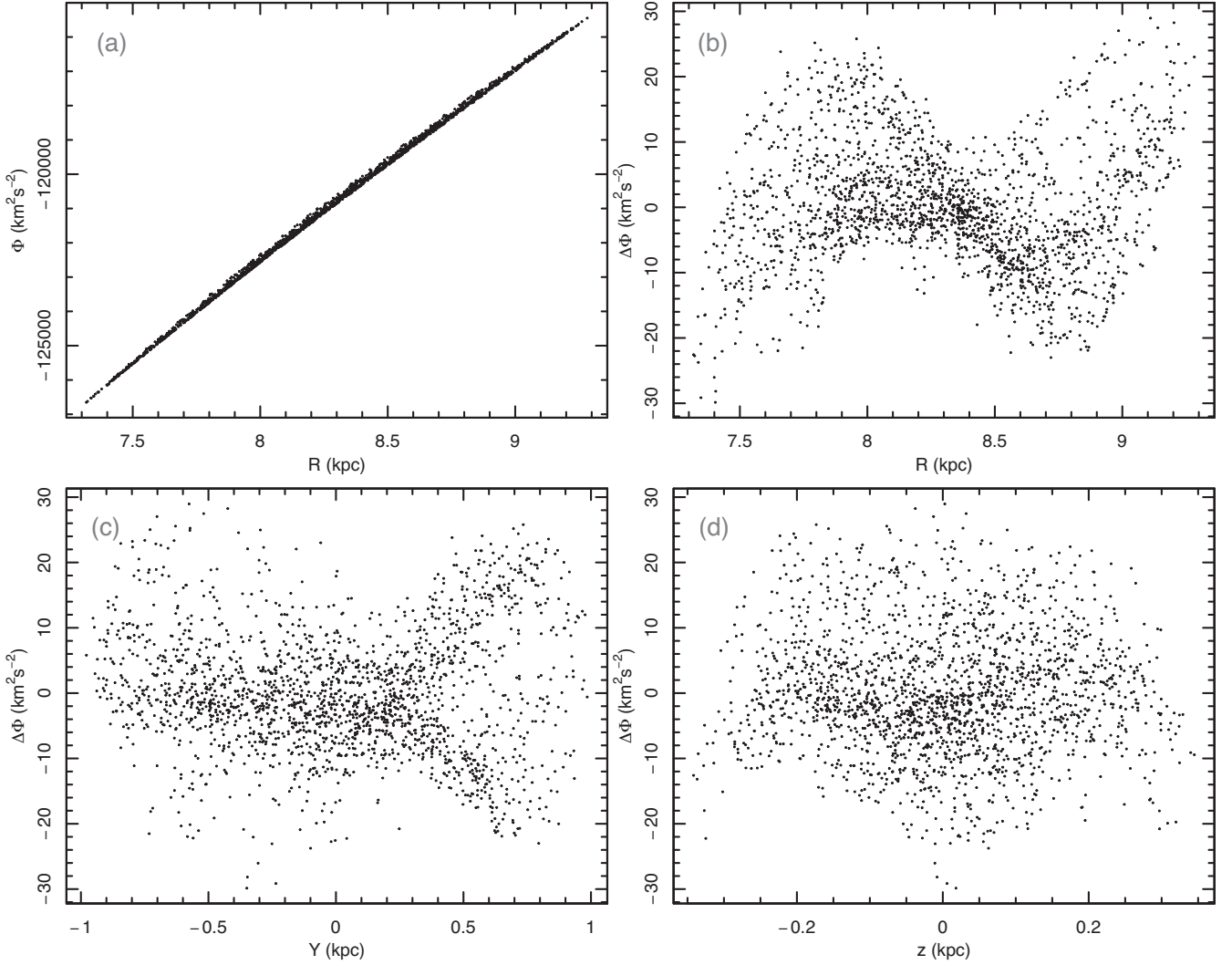


Figure 4. The adequacy of the used functional form of the acceleration field to describe potential. To avoid cluttering the figure, we plotted a subsample of 2000 points out of $\sim 60\,000$. Panel (a) shows the true potential as a function of radius; the narrowness of the correlation shows that just this dependence is the dominant source of potential variance. Panels (b)–(d) show the residuals of the true and best-fitting potential $\Delta\Phi = \Phi - \Phi_{\text{pred}}$. In panel (b) we show the radial dependence; panel (c) shows tangential dependence with Y defined as $R\Delta\varphi$; and panel (d) describes residuals in the vertical direction.

of expansion), and $A_{R,R}$, $A_{z,z}$ characterize the radial and vertical changes with radius and height above the plane. The acceleration field (18)–(20) is irrotational, hence eligible to describe the fields generated by gravity.

Acceleration field in form of equations (18)–(20) corresponds to the potential

$$\Phi = \Phi_0 + A_{R0}R + \frac{1}{2}A_{R,R}(\Delta R)^2 + A_{\theta}R\Delta\theta + A_{z,z}z + \frac{1}{2}A_{z,z,z}z^2. \quad (22)$$

We made the adequacy test for the functional form based on SR1 that contained 63 646 stars. We determined are the linear terms in expansion (18)–(20) sufficient to describe adequately potential changes in simulation data. We compared values taken from simulation (Φ) and calculated from the best-fitting test model (Φ_{pred}). Results of the test are shown in Fig. 4. Panel (a) shows the range of the true gravitational potential values Φ , which cover $11\,353\text{ km}^2\text{ s}^{-2}$. Panels (b)–(d) describe the residuals of the potential fit $\Delta\Phi = \Phi - \Phi_{\text{pred}}$. As the residuals cover the range of only $63\text{ km}^2\text{ s}^{-2}$ we may

conclude that our used functional form describes gravitational field with an accuracy of 0.6 per cent. We point out that the simulation did not contain a gas disc that may amplify the importance of vertical acceleration changes.

3.4 Modelling in a rotating reference frame

There is a technique to convert non-stationary modelling into stationary by modelling the stellar system in a rotating reference frame (e.g. Jung & Zotos 2015). Let us denote the angular speed of the reference frame as Ω_{fit} . In case $\Omega_{\text{fit}} = \Omega_p$, and a single pattern speed is sufficient to describe all the non-stationarity, then the exercise reduces to a stationary one. Although this technique is efficient in describing bar-induced non-axisymmetry, we are using it for another purpose.

When the star moves in the studied region, it spends there about ≈ 3 Myr. In case the acceleration is $\approx 6000\text{ km}^2\text{ s}^{-2}\text{ kpc}^{-1}$, the change of stars velocity is 18 km s^{-1} . For studying more subtle effects from acceleration (e.g. the acceleration caused by the bar), the changes of velocity are about $3\text{ Myr} \times 200\text{ km}^2\text{ s}^{-2}\text{ kpc}^{-1} \approx 0.6\text{ km s}^{-1}$. De-

tecting distribution shifts of this small is troublesome. In case we are modelling the system in a rotating reference frame, stars take longer to pass the studied region, the subtle acceleration effects increase, and we can make more robust inferences.

When modelling in the rotating reference frame with angular velocities Ω_{fit} , then the time average star spends in the studied region increases by a factor of $\frac{\Omega_{\text{star}}}{\Omega_{\text{star}} - \Omega_{\text{fit}}}$, where we have denoted the angular speed of an average star with Ω_{star} . The changes of acceleration from a component moving with Ω_p would decrease by the factor of $\frac{\Omega_p - \Omega_{\text{fit}}}{\Omega_p}$. In case the angular speed of the asymmetry and the angular speed of the star are similar, then the overall effect from time dependence of the potential remains the same. In subsequent sections, we provide modelling results and their dependence on the rotation of the reference frame.

3.5 Selection of the non-stationarity description

The novelty of the present analysis is an introduction of a non-stationarity in the orbital arc method. More specifically, while calculating small orbital arcs in a selected region and thereafter calculating probabilities to find a star in these orbits we introduced the term ht in equation (9). For every orbit the constant h has a certain value. In a selected region there are a multitude of orbits and probably many different values of h . For example, we cannot assume that halo and disc are similarly perturbed at SN; hence we must implement a possibility that certain orbital parameters may determine h values. Thus, although h is assumed to be a constant for a given orbit, while looking to the whole region h is a function of orbits. We assume that h is a smooth function of integrals of motion, particularly the angular momentum L_z integral. The choice of angular momentum as the dependent variable is motivated by the results of Antoja et al. (2018) where they show substructure comes forth by analysing rotational velocities (in case of small regions, rotational velocity and angular momentum L_z have almost one-to-one relation). The functional form for h we selected in a way that most stars are populating their orbits stationary, but some with a certain angular momenta have elevated to non-stationarities:

$$1 + ht = 1 + h(L_z)t = 1 + h_{L_z} \exp \left[-\frac{(L_z - L_{z0})^2}{L_{z\sigma}^2} \right] t. \quad (23)$$

The L_{z0} describes the angular momentum value around which orbits are populated most non-stationarily. The σ_{L_z} shows the spread of the non-equilibrium orbits, and the h_{L_z} shows the maximum level of non-stationarity of orbits.

3.6 Implementation of mock modelling and conclusions

To test the limits of the method, we modelled the mock data repeatedly with parameters emphasizing different aspects of the model. These aspects include the rotation of the reference frame (selection of Ω_{fit}), description of non-stationarity (selection of h), and inclusion of systematic effects (selection of C).

First two aspects are interrelated. The average angular speed of the region is $\Omega_{\text{star}} \approx 25 \text{ km s}^{-1} \text{ kpc}^{-1}$. To increase the time stars spend in the region the Ω_{fit} should be as close to $25 \text{ km s}^{-1} \text{ kpc}^{-1}$ as possible. But let us look closer. If $\Omega_{\text{fit}} = 0$ all the stars in the disc region enter the region from one side and exit from the other. Once Ω_{fit} approaches Ω_{star} , the stars exit the studied region in a random direction. If $\Omega_{\text{fit}} > \Omega_{\text{star}}$ stars move in the region in reverse compared to the region that stands still. But now issue arises in the interpretation of h in the modelling. We wish to keep the interpretation $h \approx (\partial f / \partial t) / f$, but this relation does not hold well if $\Omega_{\text{fit}} \neq 0$ as the orbit extrapolation

‘meet’ different sets of stars for Ω_{fit} values. Only in case the h is a very smooth function of integrals of motion, the relation still holds.

Thus, we selected priors for the parameters in analytical form of h (equation 23) accordingly. The L_{z0} had to be within the 10 and 90 percentiles of the stellar angular momenta so that in case of zero perturbations, there would be no degenerate solutions in ranges where there are no stars. The width of the distribution for angular momenta of the non-equilibrium was between $L_{z\sigma}$ 100 and $700 \text{ km s}^{-1} \text{ kpc}$, and the h_z value was $\pm 50 \text{ Gyr}^{-1}$. During the mock data modelling, we did not reach these prior limits.

3.6.1 Conclusions from the acceleration modelling

We made five different fittings of mock data. In each case we had 12 regions. The results are given in Figs 5 and 6. Overall, it seems that calculation of a_R is more biased and is more difficult to fit, hence we mostly emphasize our analysis based on a_R . The analysis based on a_θ is very similar.

First, we modelled SRs in a non-rotating reference frame ($\Omega_{\text{fit}} = 0 \text{ km s}^{-1} \text{ kpc}^{-1}$) without considering systematic errors ($C = 1$) and assuming stationarity ($h = 0$). These results are depicted as red circles in Figs 5 and 6. One can see that in four cases (2, 3, 5, and 8), the fit is quite good, and the model and actual value differences are within 1σ uncertainties. In addition, in three cases (6, 9, and 12) differences are within 2σ uncertainties. In regions 1, 4, 7, and 11 the uncertainty is clearly underestimated. Let us look at the positions where the regions situate from Fig. 2. In a strongly barred galaxy, we would expect that regions that are 180° shifted should give a mismatch that matches the initial ones exactly. This matching will only happen if the bar or its induced non-equilibrium is the cause of the offset. In our case, the region pairs that are 180° off are 1–7, 2–8, etc. For the pair 4–10, region 4 has a high mismatch, while the other is $\approx 2\sigma$ offset. For the 1–7 pair, also one offset is significantly higher than the other, for the pair 11–5, the offsets also do not match at all. As these offsets do not match, we conclude that it is more likely that the origin of these offsets is not physics related but noise and sampling related.

Next, based on the non-rotating stationary modelling, we estimated the level of systematic uncertainties that statistical uncertainties do not cover. We applied the recipe described in Section 3.2.2 to estimate that likelihood ratios should be multiplied by a certain constant C . The numeric values of C are calculated based on comparing modelling results without systematic uncertainties ($C = 1$, red circles) and their distances to the actual values (green lines). Using C as a free parameter we selected C values that cover the offset best. In Table 1, we present the C value calculated based on acceleration component differences from actual value $A - A'$ and σ_{stat} values to fit the expectation $\mathbb{E}(A - A')^2 = \sigma_{\text{stat}}^2 + \sigma_{\text{sys}}^2$. Since the values differ for different parameters, we select the value in between of most important parameters we would like to recover precisely: A_R and A_θ . Then we adopted the value $C = 0.13$ and calculated accelerations again. Corresponding accelerations are depicted by orange circles.

Next, we test the influences of the speed of the reference frame. In the figures, we show the modelling with condition $\Omega_{\text{fit}} = \Omega_p = 37 \text{ km s}^{-1} \text{ kpc}^{-1}$ with light blue circles and results are clearly better for the regions that had previously substantial offset from the actual value (see especially regions 1, 4, 6, 7, and 10). The only exceptions are regions 5, 8, and 9.

For the next test, we add the non-equilibrium possibility to the modelling ($h \neq 0$). We depict the non-equilibrium models as dark blue circles in the figures. Comparing the results with the corresponding stationary version (orange circles), we do not see

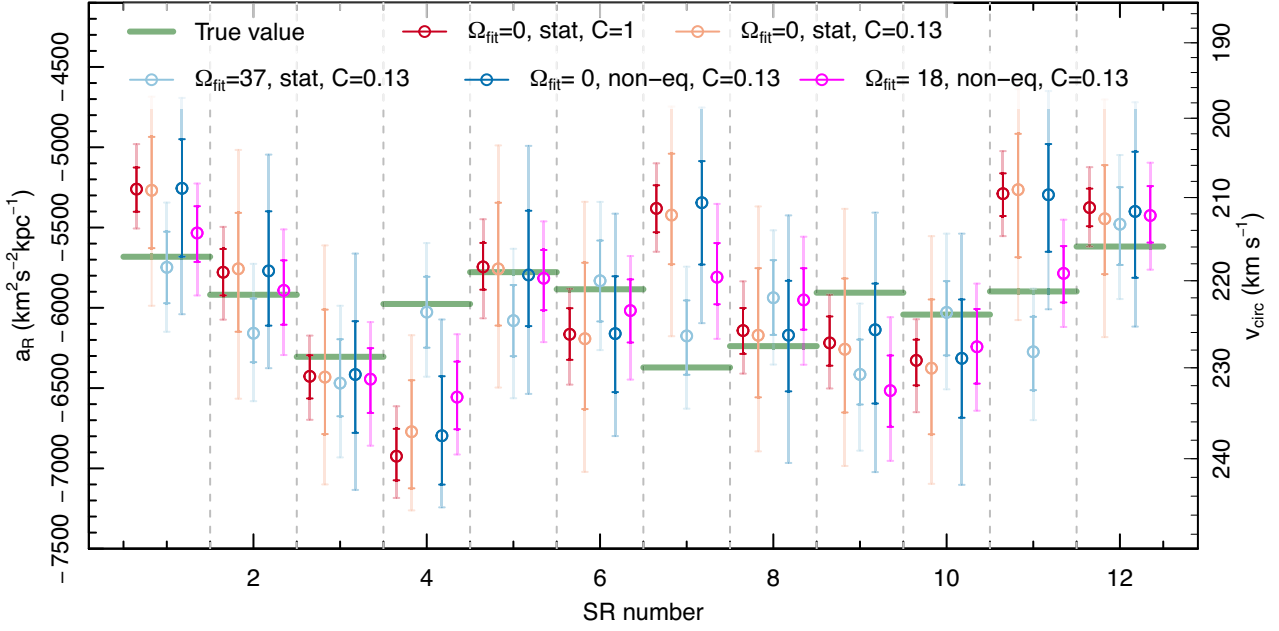


Figure 5. The recovery of radial acceleration a_R from modelling simulated data. For each region, we present a set of results from different modellings with 1σ and 2σ uncertainties. For each region, from the left, corresponding points are: (1) non-rotating reference frame in stationary modelling to estimate systematic uncertainties; (2) the test how well the inclusion of systematic uncertainties works; (3) modelling in case of the reference frame corresponding to the pattern speed; (4) non-stationary modelling where the relation $h \approx (\partial f / \partial t) / f$ holds well; and (5) modelling with the best-fitting parameter set.

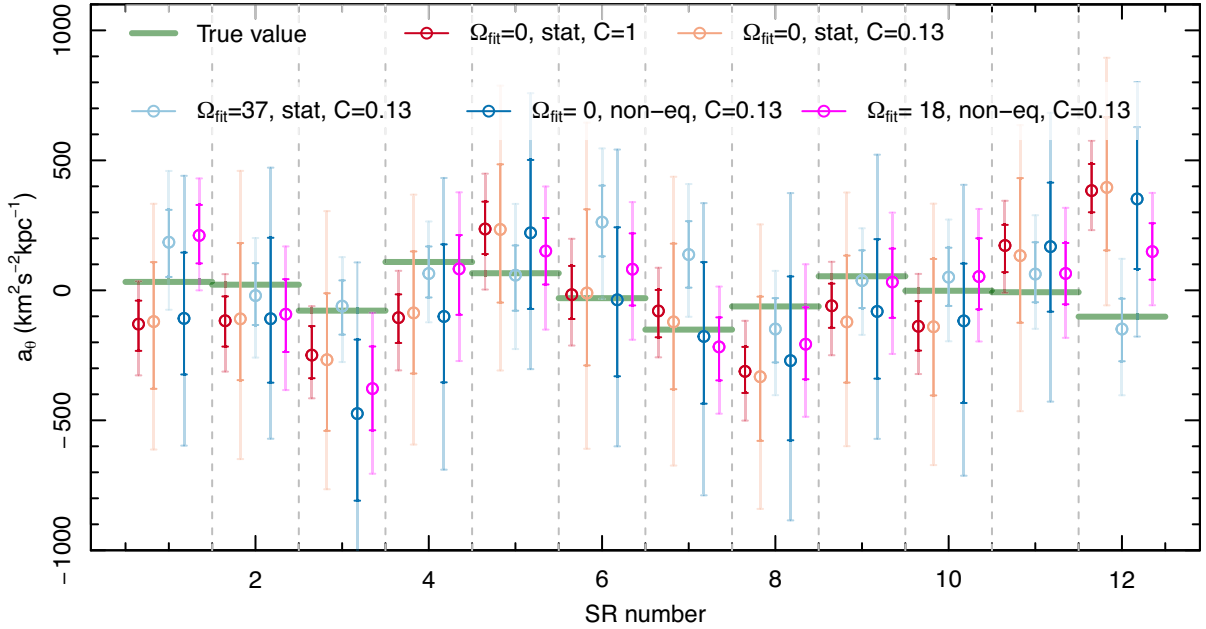


Figure 6. Same as Fig. 5, but calculated based on recovery of a_θ .

Table 1. The C values calculated based on different acceleration components. Values over 1 indicate that the statistical uncertainty was overestimated from the modelling.

Variable	A_R	$A_{z,z}$	A_θ	$A_{R,R}$	A_z
C	0.088	2.26	0.20	0.57	3.3

significant changes. We conclude that in the $R \approx 8$ kpc regions, the non-equilibrium has less significance than effects from acceleration. An alternative explanation is that the number density of stars is too little to model in such depth that the non-equilibrium starts to dominate over acceleration components in a small region. The third explanation is that the functional form of h is not sufficiently diverse to describe actual non-equilibrium. In the next section, we will dissect the recovered non-equilibrium values more thoroughly.

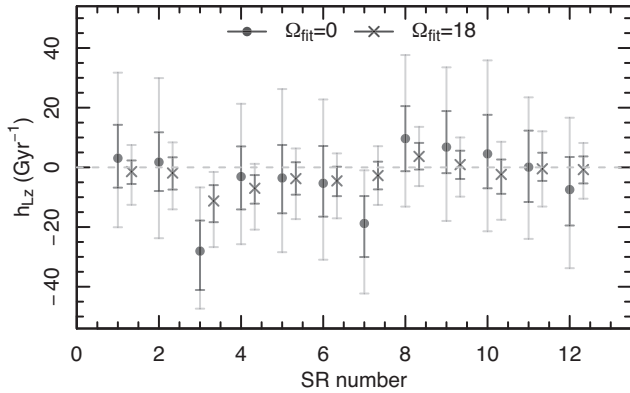


Figure 7. The fitted h_{L_z} parameter values and uncertainties for modelling in both non-rotating and rotating reference frames. One can notice a bias toward lower absolute values, which is expected to be ≈ 3.6 times compared the rotating and non-rotating frames (see main text).

In the last test run, we adapted $\Omega_{\text{fit}} = 18 \text{ km s}^{-1} \text{ kpc}^{-1}$ to maximize the time star spends in the studied region, included non-stationarity and used the $C = 0.13$ value (magenta circles). We could recover the actual values well in nine cases. In the case of the three problematic regions (4, 7, and 11) the $\Omega_{\text{fit}} = \Omega_p$ gives better results in two cases, while in SR11, the $\Omega_{\text{fit}} = 18 \text{ km s}^{-1} \text{ kpc}^{-1}$ is better. Overall, we conclude that we can adequately recover acceleration in most cases, and if the mismatch is caused by sampling noise, we do not expect similar problems in the observational application.

3.6.2 Conclusions from the non-equilibrium modelling

We included the non-equilibrium term h for $\Omega_{\text{fit}} = 18$ and for $\Omega_{\text{fit}} = 0$. In both cases, we calculated a set of parameters that describes the systems underlying non-equilibrium. Before discussing derived results we would like to note what to expect when modelling non-equilibrium in a rotating reference frame.

Let us imagine a density gradient caused by non-equilibrium. Densities are proportional to time (oPDF) and time in a studied region is determined by the region's size and the velocities. As we use at present angular velocities let us denote the $\Delta\varphi$ as the angular size of the studied region. Then for an average star, it would take $t_0 = \Delta\varphi/\Omega_{\text{star}}$ to leave the region. In a rotating reference frame, the time would be $t_r = \Delta\varphi/(\Omega_{\text{star}} - \Omega_{\text{fit}})$, indicating that times and hence also density gradient would be increased by a factor of $\approx \Omega_{\text{star}}/(\Omega_{\text{star}} - \Omega_{\text{fit}})$. As times needed to produce a gradient would change by this factor, the h values should also be modified by the same amount. These considerations are not rigorous, nor are they intended to be, as not all motions in the disc are rotation dominated, especially in a rotating reference frame where $\Omega_{\text{fit}} \rightarrow \Omega_{\text{star}}$. In case of $\Omega_{\text{fit}} = 18$ that is used in simulations the factor $\Omega_{\text{star}}/(\Omega_{\text{star}} - \Omega_{\text{fit}})$ is ≈ 3.6 .

In Fig. 7, we provide the amplitude values of the function $h(L_z)$ (see equation 23) for $\Omega_{\text{fit}} = 0$ and $\Omega_{\text{fit}} = 18$. We see that the $\Omega_{\text{fit}} = 18$ based values are closer to zero line than the $\Omega_{\text{fit}} = 0$ based values. Based on the considerations from the previous paragraph, this is expected. But we see also that most of the values are in fact zeros within the error. This means that in the simulation, the regions at $R = 8.3 \text{ kpc}$ are not sufficiently perturbed to recover the perturbation from such a small region. Thus, the levels of non-equilibrium are smaller than $|(\partial f/\partial t)f^{-1}| \lesssim 0.03 \text{ Myr}^{-1}$ or 3 per cent Myr^{-1} .

The h_{L_z} is just one parameter describing the non-equilibrium function h . The entire function is shown in Fig. 8 in case of the

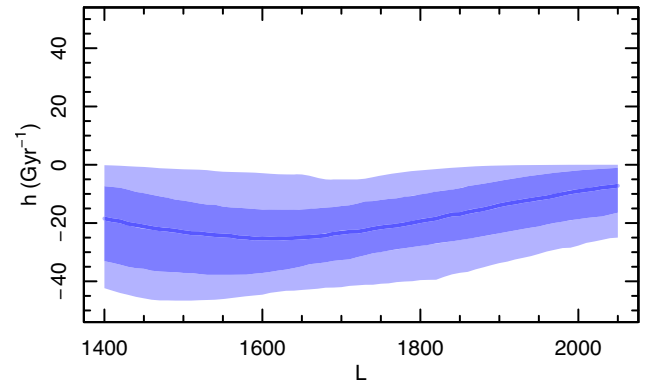


Figure 8. Distribution of h as a function of angular momentum L_z for the mock SR3. The blue colours describe the median value, $\pm 1\sigma$ and $\pm 2\sigma$ regions. These regions are calculated by constructing single lines of posterior parameter samples and selecting their quantile lines. Hence, they do not have to follow the equation (23).

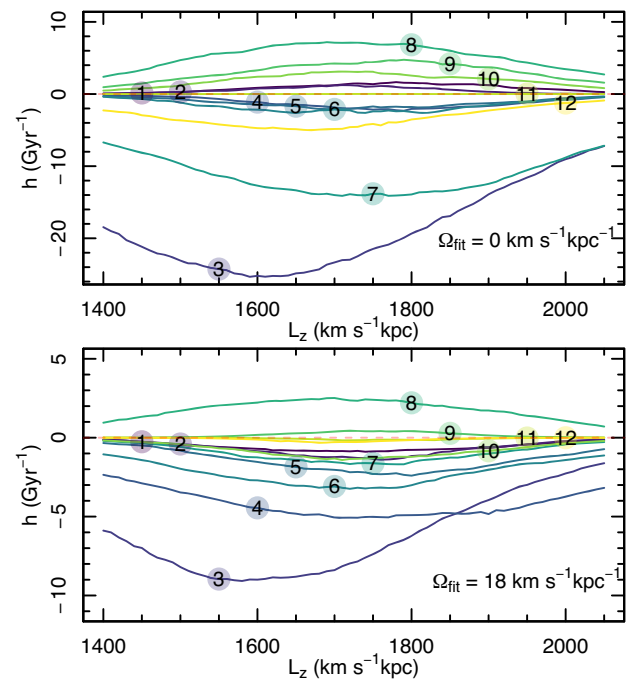


Figure 9. The medians of the function h for all regions as a function of angular momentum L_z . Region numbers are in the circles on top of each line. The top panel shows results for modelling in case of $\Omega_{\text{fit}} = 0$, and the bottom one for $\Omega_{\text{fit}} = 18 \text{ km s}^{-1} \text{ kpc}^{-1}$. The differences of ~ 3.6 times are expected due to the rotation of the reference frame.

region SR3 (non-rotating frame). We picked this region as it had a large h_{L_z} value. The median and uncertainty corridor is constructed by calculating all the $h(L_z)$ function lines from the MCMC posterior points and estimating quantiles of each L_z value. It is seen that h values are negative in this region.

In Fig. 9, we show the median lines of all the regions, not just one as in Fig. 8. Again, we see that h values depend strongly on the Ω_{fit} values as described earlier in this section. The ones that are modelled with $\Omega_{\text{fit}} = 0$ are the ones that have the interpretation $h \approx (\partial f/\partial t)f^{-1}$. We see from the top panel, that h values make a decreasing trend between SR8 and SR12. A similar trend is seen also between SR1 and SR6 (except for SR3). It seems that over half of the galaxy,

the phase-space density grows due to non-equilibrium and over the other half, it decreases (see Fig. 2). This trend is similar to the $m = 1$ asymmetry, but for $\partial f/\partial t$. The $\Omega_{\text{fit}} = 18$ modelling semiconfirms it, but one should keep in mind that 1:1 relation between $\Omega_{\text{fit}} = 18$ and $\Omega_{\text{fit}} = 0$ holds only in case of zero-dispersion dynamics, which is not the case. Because of weak statistical significance, we are not able to make any firm conclusions about it.

4 NON-STATIONARITY OF THE MILKY WAY IN THE SOLAR NEIGHBOURHOOD FROM GAIA DR2 DATA

In Kipper et al. (2020) we used the orbital arc method to calculate the acceleration field in the solar neighbourhood (SN). The model was a stationary one. In this paper (see Section 2), we improved the method to include also possible non-stationarities of the galaxy. Here we remodel the SN region to find out how perturbed region we are living in. Test of the method with mock data presented in Section 3 confirmed us that the method allows us to conclude that the method is reliable.

For the solar velocity we use the latest values that are based on *Gaia* Early Data Release 3 (EDR3) reflex motion minimization (Malhan, Ibata & Martin 2020); the values are $V_{\odot,R} = 8.88 \text{ km s}^{-1}$, $V_{\odot,\theta} = 241.91 \text{ km s}^{-1}$, and $V_{\odot,z} = 3.08 \text{ km s}^{-1}$.

4.1 Implementation of the modelling with *Gaia* data

We use a similar data set as in Kipper et al. (2020): the region is a flux-limited (in J band up to 10.25^m) oblate spheroid, with semiheight of 0.4 kpc and radius 0.494 kpc containing 525 264 stars from *Gaia* DR2 (Gaia Collaboration 2016, 2018) with STARHORSE (Anders et al. 2019) distance estimations. The size of the region determines the time-scale for how long the non-stationarity estimates can be handled as valid and be extrapolated. The average velocity of stars in the region is about $\approx 240 \text{ km s}^{-1}$ and the diameter of the region is $\approx 1 \text{ kpc}$, causing stars to be in the region for $\lesssim 4 \text{ Myr}$. This is the maximum time interval the derived estimates for the non-equilibrium parameter h should be used.

To use the orbital arc method, one needs as an input all six phase-space coordinates of stars. As the *Gaia* observations provide at present radial velocities for only a moderate number of stars it observes, this causes a selection bias. For stars with $m_g \simeq 4^m$ about 50 per cent of stars have a measured radial velocity, while for stars with $\simeq 11^m$ the completeness is ~ 80 per cent (see Katz et al. 2019). In addition, there is a significant direction dependence. In the previous paper (Kipper et al. 2020), we used a match with the Two Micron All-Sky Survey (2MASS) magnitudes that are not attenuation sensitive and constructed data set for modelling is based on these.

In the previous paper, we adapted a flux-limited approach by choosing a superposition of volume-limited samples. We added a similar cut to cope with the bright-end selection: we removed all the stars that are fainter than some bright-end J -band magnitude limit (J_{BE}). The validity of this procedure is the same as when cutting the dim end of the sample, and the reasoning is more thoroughly covered in Kipper et al. (2020). Removal of the bright end is done in the same way in modelling: the orbit is integrated until the star exits the studied region or its brightness is not between the used magnitude limits. Although it provides the same overall results, the accuracy of the model is more diminutive. As an illustration we present in Fig. 10 two (oversimplified) cases: one where an orbit runs through the region intact and the case where the brightness limit ‘cuts’ the orbit into two. In the right-hand panel, we provide the

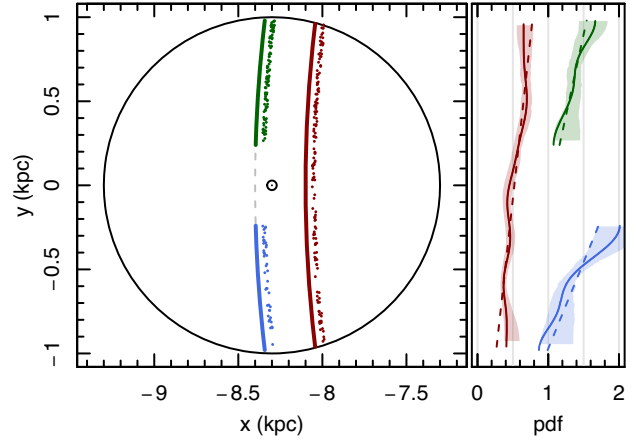


Figure 10. An illustration of a side effect of the bright-end sample cut. The left-hand panel shows how the brightness limit splits an intact orbit (the red one) into two (green and blue ones) by getting too close to the Sun so that apparent magnitude increases. The stars are populated along the orbit (but shifted for illustration purposes) to mimic the non-equilibrium density population. The right-hand panel shows the probability density functions (PDFs) along the y -direction, dashed line as the slope data were generated with. Differences of slopes are apparent due to not normalization to 1. One can notice higher uncertainties in case the orbit is split (the wavy sampling noise do not cancel out sufficiently), causing an overall hindrance in modelling.

density distributions and the corresponding uncertainty corridor for both cases, along with the actual slope we generated the data. As the split orbital PDF distribution has higher uncertainties than the unsplit one, the overall modelling through these is more uncertain, and the overall accuracy of the model is reduced. We used two different limits J_{BE} : 9^m (default) and 7^m (denoted as less conservative). The former sample contains 352 656 stars and latter one 481 464 stars.

As the selection function has a significant impact on data distribution, we added a supplementary way to cope with it. For the orbit calculations, we multiplied the h with a term $h_{\text{selection}}$, which is an inverse of the fraction of stars observed compared to completeness, hence after division, we get the incompleteness-corrected orbital populations. Based on the Katz et al. (2019) results, we approximated it to be a linear function of apparent magnitude $h_{\text{selection}} = h_{s0} + h_{s1}m$. Hence, a stellar orbit is populated with the density

$$\rho \propto dt(1+h)(h_{s0}+h_{s1}m), \quad (24)$$

where m is the apparent magnitude of that orbital point.⁴ Again, due to the normalization of PDF of each orbit, we selected h_{s0} to be 1. The parameter describing the selection (h_{s1}) is a free parameter in modelling. We expect it not to be confusable with physical non-equilibrium as it influences orbital densities with spherical symmetry around the Sun, compared to along the rotation for non-equilibrium.

The modelling is done in a similar manner as we tested the method with mock data (Kipper et al. 2019), although the statistical inference at present is done with a finer grid using $30^2 = 900$ grid cells $G = 32$ times. We set a limit that no cell should have less than 10 stars to avoid too small grid cells, and high relative Poisson noise. The likelihood is maximized using MULTINEST (Feroz & Hobson 2008; Feroz et al. 2009, 2019) code with 100–500 live points. We modelled the region with parameter $C = 0.13$ from equation (16), which might

⁴Apparent magnitude is determined based on solar location, and the absolute magnitude of the star that’s orbit is being calculated.

Table 2. Calculated accelerations and perturbation levels in solar neighbourhood (SN). In the first two columns assumed angular velocity of the reference frame and limiting J -band magnitude are given, in subsequent five columns acceleration field coefficients are given, in the last column perturbation amplitude parameter h_{Lz} is given.

Ω_{fit} ($\text{km s}^{-1} \text{ kpc}^{-1}$)	J_{BE} (m)	A_R ($\text{km}^2 \text{ s}^{-2} \text{ kpc}^{-1}$)	A_θ ($\text{km}^2 \text{ s}^{-2} \text{ kpc}^{-1}$)	A_z ($\text{km}^2 \text{ s}^{-2} \text{ kpc}^{-1}$)	$A_{R,R}$ ($\text{km}^2 \text{ s}^{-2} \text{ kpc}^{-2}$)	$A_{z,z}$ ($\text{km}^2 \text{ s}^{-2} \text{ kpc}^{-2}$)	h_{Lz} (Gyr^{-1})
0	9	-6502^{+605}_{-539}	-304^{+331}_{-360}	223^{+169}_{-237}	494^{+1670}_{-1544}	-3012^{+1671}_{-1709}	-13^{+49}_{-43}
0	7	-6462^{+273}_{-238}	-348^{+196}_{-200}	191^{+129}_{-121}	262^{+1237}_{-1333}	-2789^{+1196}_{-1193}	79^{+59}_{-52}
20	9	-6354^{+198}_{-198}	-245^{+124}_{-118}	106^{+94}_{-102}	-237^{+1065}_{-899}	-2888^{+714}_{-788}	-7^{+17}_{-22}
40	9	-6253^{+231}_{-237}	119^{+178}_{-219}	-93^{+136}_{-135}	-895^{+1001}_{-745}	-3073^{+954}_{-976}	-15^{+22}_{-43}

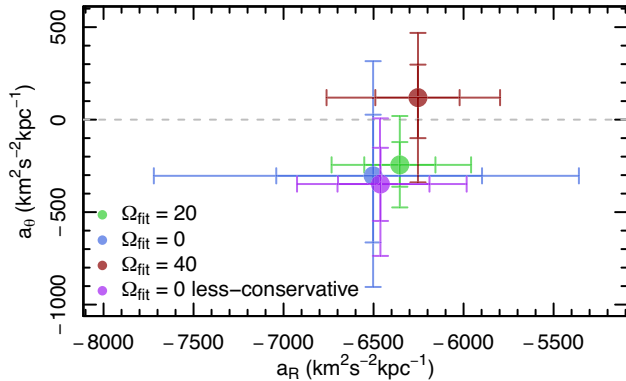


Figure 11. The two main components of recovered acceleration field. The horizontal axis shows radial, and vertical axis shows tangential acceleration components. Different colour lines show modelling results in different reference frames or selection limits. We provide both 1σ and 2σ uncertainties.

give overestimated uncertainties in case the cause of uncertainties is sampling noise.

As the SN region is quite far from the bar, the acceleration field should be sufficiently well described with a simple analytical form. Hence, we select the form (18)–(20) to describe the acceleration field. For the non-equilibrium term, we used the same form as in simulation data equation (23).

We used three different reference frames when modelling: $\Omega_{\text{fit}} = \{0, 20, 40\} \text{ km s}^{-1} \text{ kpc}^{-1}$. These values provide results where we emphasize the recovery of non-equilibrium parameters or acceleration parameters. The values differ slightly from the ones we used in mock analysis since the velocities of MW are slightly larger. We chose the $\Omega_{\text{fit}} = 20 \text{ km s}^{-1} \text{ kpc}^{-1}$ since MW stellar angular velocity is $\approx 29 \text{ km s}^{-1} \text{ kpc}^{-1}$ and based on the mock results we chose the Ω_{fit} to be less than this value, but still large enough to increase the time stars spend in the region in a rotating reference frame.

4.2 The non-stationarities in the solar neighbourhood

Modelling the SN by including non-stationarities, we can update the values of acceleration and assess the importance of non-stationarities. We show the calculated acceleration field in Table 2 and the main components of it in Fig. 11.

For the radial acceleration A_R we found the weighted mean of all the radial accelerations in Table 2 to be $\langle A_R \rangle = -6360 \text{ km}^2 \text{ s}^{-2} \text{ kpc}^{-1}$. All different implementations of the modelling (mostly the angular speed of the reference frame Ω_{fit}) give consistent results. Derived $\langle A_R \rangle$ corresponds to the circular velocity of 228.4 km s^{-1} , which is slightly less than the usual ones from the literature (e.g. $v_c = 238 \pm 9 \text{ km s}^{-1}$ from Schönrich 2012). The

main reason is the difference of the used solar motion, Malhan et al. (2020) compared to Schönrich (2012), being 10.33 km s^{-1} . Taking this into account the circular velocities are consistent with each other. The radial acceleration derived in Kipper et al. (2020) was $-6214 \text{ km}^2 \text{ s}^{-2} \text{ kpc}^{-1}$. The main difference between these results is the inclusion of non-equilibrium. We can conclude that the equilibrium assumption gives in the SN case the difference by ~ 2 per cent for radial acceleration.

The average tangential acceleration $\langle A_\theta \rangle$ is $-201 \text{ km}^2 \text{ s}^{-2} \text{ kpc}^{-1}$. Contrary to the radial accelerations, the tangential ones varied clearly more between different modelling implementations. In order to find out which implementation is a preferred one, let us remind our tests with mock data. In Fig. 6, we provide the recovery precision for different modelling settings. Comparing the cases where Ω_{fit} is 0, 18, or $37 \text{ km s}^{-1} \text{ kpc}^{-1}$, the results are mostly similar, but still in some cases differ. The differences are largest for cases where the rotation of the frame matches the bar pattern speed: mostly $\Omega_{\text{fit}} = \Omega_{\text{bar}}$ has a similar, better, or significantly better fit than others; however, in two cases (regions SR6 and SR7) fits are worse or significantly worse. Based on the mock analysis, we saw that the average consistency is improved when Ω_{fit} is close to stellar velocity. Taking this into account, we favour the results with $\Omega_{\text{fit}} = 20 \text{ km s}^{-1} \text{ kpc}^{-1}$, i.e. $A_\theta = -245^{+124}_{-118} \text{ km}^2 \text{ s}^{-2} \text{ kpc}^{-1}$. If the torque from the bar causes this acceleration, then this acceleration corresponds to the mass of the bar of $1.3 \times 10^{10} M_\odot$ (see details from Kipper et al. 2020 with the assumed bar density profile from Wegg, Gerhard & Portail 2015).

Let us introduce the parameter h_{s1} describing a mismatch due to apparent magnitude cut caused by the selection function. The numeric value we model for the h_{s1} is quite uncertain but has an average ≈ -0.01 . In modelling, the value does not drop below -0.025 but can be as high as 0.1 in the posterior sample. For the interpretation, the average numeric value h_{s1} the bright-end and dim-end selection (extreme values) gave number density differences of 1.5 per cent or 3.5 per cent, depending on the used apparent magnitude limit for selection. From the vast range of acceptable values to the modelling and no correlation between acceleration parameters and h_{s1} , we conclude that the selection function did not contribute significantly to the modelling.

While describing the mock data modelling (Section 3.4) we mentioned that when handling Ω_{fit} and function h one needs to distinguish two separate cases: one where the $\Omega_{\text{fit}} = 0$ and the other where $\Omega_{\text{fit}} \neq 0$. In the first case it is possible to use the interpretation $h \approx f^{-1} \partial f / \partial t$ giving a physical interpretation to the perturbations. In the non-zero cases, the interpretation is not valid, and the non-equilibrium part is only used to sieve out acceleration effects from all of the effects. We provide the resulting non-equilibrium function in Fig. 12. In the top panel, we show the $\Omega_{\text{fit}} = 0$ cases. One can see that the levels of non-equilibrium needed to make the data in the region self-consistent can be quite large compared to the one in

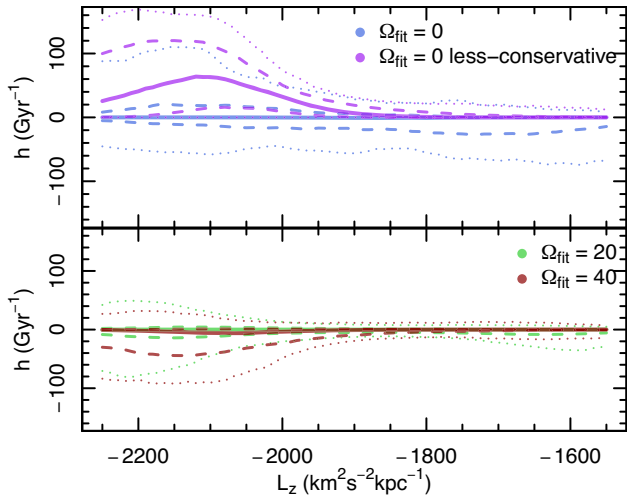


Figure 12. The levels of calculated non-equilibrium function $h(L_z)$ in SN. Dotted thin lines show $\pm 2\sigma$, dashed ones $\pm 1\sigma$, and continuous line gives the median values similar to Fig. 8. The top panel shows the results where $h \approx \partial f / \partial t$ interpretation holds, the bottom ones where it does not (and is even reverse, see Section 3.6.2).

the simulated galaxy (see Fig. 9). It is also seen that the level of the detected non-equilibrium is dependent on the sample brightness limit – the brightness limit determines the sample size and the extent of stellar orbits (see Fig. 10 for clarification). If we do not use a bright-end cut at all, the level of perturbations increases even more. Although both selection effects and real non-equilibrium can produce the same outcome, we favour the real non-equilibrium since the selection effects induced by magnitude limits produce spherically symmetric over- or underestimation of densities. In contrast, a non-equilibrium population along the orbit would produce linear ones along the rotation direction. Therefore these effects are independent and distinguishable when the observer is in central parts of the region. Overall we consider our main results based on the $\Omega_{\text{fit}} = 0$ modelling with less conservative selection. We consider these not being biased by brightness and having clear physical interpretation.

The derived h -values in cases of real MW data and of mock simulation data are different in their magnitude. For observations, the levels of non-equilibrium are larger than simulations. We used the simulation of Garbari et al. (2011) that contained dark matter and stellar particles and neither mergers nor gas particles. The lack of these two contributions can explain the excess of h in observations. We can see from the Fig. 12 that the maximum of h is around $L_z \approx -2100$, which translates to rotation speeds of the non-equilibrium orbits $\approx 255 \text{ km s}^{-1}$, which is faster than the circular speed equivalence of this region ($\approx 230 \text{ km s}^{-1}$). It indicates that these stars that have a non-equilibrium population along the orbits originate further away on average, and in the studied region, they are closer to their pericentre than apocentre. An alternative interpretation would be that non-equilibrium is induced by the gas disc that rotates faster than average stellar disc (due to asymmetric drift). The disc gas comoves with faster moving stars, and the non-equilibrium could be induced by gas distribution inhomogeneities.

5 DISCUSSION

In this paper, we demonstrate the capabilities and perspectives of inclusion of non-stationarities in modelling of the MW galaxy. First, based on our tests on simulation data, we conclude that the inclusion

of non-stationarity to the modelling does not produce any additional inaccuracies to the model and helps to derive the acceleration field in perturbed states of a galaxy. Applying the developed modelling method to *Gaia* data in SN demonstrates the ability of the method to detect perturbations, calculate their properties, and possibly pinpoint their possible origin.

The applications in this paper studied regions of size 0.5–1.0 kpc. We selected the small regions in order to have a minimally simple form to the acceleration. Would the regions be larger, the acceleration field should be more complex. In the mock application, the functional form is adequate to cover the gravitational potential changes (see Fig. 4), only in the case of radial acceleration, there is hint to a systematic trend in order to have additional acceleration term. We did not include it in present case since the systematic effects describe deviations in the order of $\pm 20 \text{ km}^2 \text{ s}^{-2}$, while the overall potential changes are $\sim 10\,000 \text{ km}^2 \text{ s}^{-2}$. Would a dense gas disc be present, then the acceleration would have more abrupt changes in the vertical direction. This would favour an additional term to a simple linear approximation.

Although selecting larger regions poses some calculation difficulties due to more complicated acceleration field form, it provides also advantages. Selecting a larger region allows orbital arcs to be longer when passing through the region, and inference allows larger number density of orbits. Since the density of orbits is larger, the causal connection between different parts of the regions is tighter, and inference of non-equilibrium ($\partial f / \partial t$) is more robust. Larger regions also pose tighter constraints on the stability of the gravitational potential, which we will dissect in the next paragraphs.

In principle, in a non-stationary system gravitational potential is a function of time. However, in this paper we assume that density perturbations are small and do not contain significant amount of mass. Thus, we assume that potential and acceleration fields formulae do not contain time component (see Section 2.1). We are modelling only non-stationarity of the density. Thus we assess now how accurate this assumption is using the simulated data. When calculating stellar orbits in a selected region potential changes in time because the position of the region changes with respect to the overall asymmetries of the galaxy. Fig. 13 shows the acceleration components as a function of the position in the galaxy, more specifically, as a function of the position angle measured at $R = 8.3 \text{ kpc}$. We see that accelerations change by up to $\sim 300 \text{ km}^2 \text{ s}^{-2} \text{ kpc}^{-1}$ as a star circles the entire galaxy. As the region limits the extent of stars position range, corresponding accelerations vary less. Let us estimate expected acceleration changes due to change of the potential.

The radius of the studied region is about 1 kpc and semiheight 0.35 kpc. The average rotational speed in the SRs is $\approx 210 \text{ km s}^{-1}$, indicating that it takes $\Delta t \approx 3 \text{ Myr}$ for a random star in the studied region to reach the boundary of the region. This estimate includes reducing sizes due to the flattened geometry of the region but ignores the dispersion component of the velocities.

Let us denote Ω_p as the angular speed of the asymmetries that cause changes of acceleration. For bar, it is $\Omega_p \approx 37 \text{ km s}^{-1} \text{ kpc}^{-1}$ (see Section 3.1). The angle (measured from the centre of the galaxy) from the bar tip changes by the time an average star passes the studied region $\Delta\theta = \Omega_p \Delta t \approx 6^\circ$. The corresponding value for the SN region of the MW is $\Delta\theta_{\text{obs}} = 3^\circ$. It is smaller due to smaller extent of the SN region. The top left-hand part of the top panel of Fig. 13 shows these values as lengths of horizontal bars. The bottom panel of the figure shows how much accelerations change with this rotation angle. There is a significant dependence where the studied region is located in the mock galaxy. Although there is a dependence, the order of magnitude is low compared to the mean radial acceleration. The

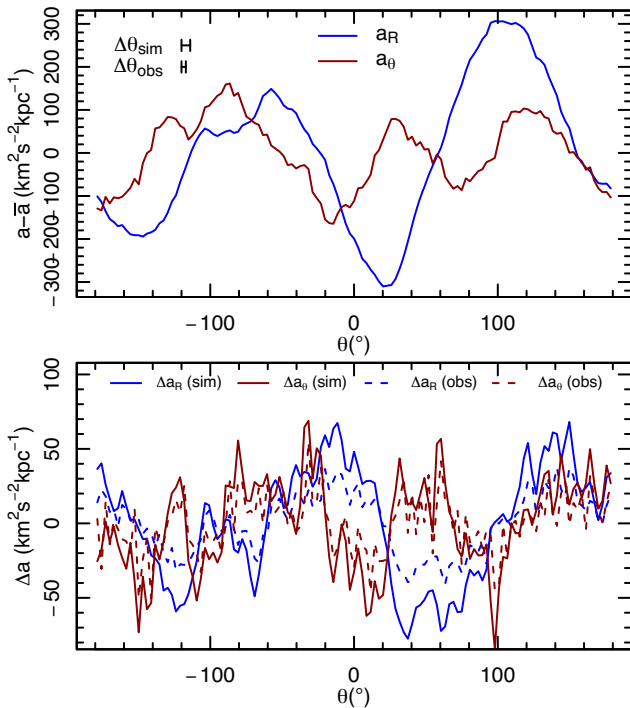


Figure 13. The position dependence of acceleration components over the simulated galaxy. The top panel shows the mean-subtracted acceleration as a function of angle measured at the centre. We can see that the acceleration components can deviate from axisymmetry up to levels $300 \text{ km}^2 \text{ s}^{-2} \text{ kpc}^{-1}$. The change of studied region position with respect to these asymmetries causes the potential to be time dependent. The top left-hand part shows the expected change of position ($\Delta\theta$) when a star passes through the studied region. The bottom panel shows the change of acceleration with the time a star passes through the studied region. It is in the order $\Delta a \lesssim 50 \text{ km}^2 \text{ s}^{-2} \text{ kpc}^{-1}$.

absolute mean of the components describes how much change for the acceleration (Δa) we expect when the star passes the studied region. For simulations $\Delta a_R \approx 33$ and $\Delta a_\theta \approx 26 \text{ km}^2 \text{ s}^{-2} \text{ kpc}^{-1}$, and when assuming similar acceleration distribution for MW than the simulation has, then the corresponding values are $\Delta a_R \approx 17$ and $\Delta a_\theta \approx 15 \text{ km}^2 \text{ s}^{-2} \text{ kpc}^{-1}$. The reduced size of the studied region is the cause of the less sensitivity to the time dependence of the potential. These values show that the time dependence can cause acceleration changes in the order of $33/6000 \approx 0.5$ per cent, which we consider insignificant for this type of modelling and conclude that the orbital arc method is insensitive to the gravitational potential time variations in case of small regions of interest.

The case of consistent stationary systems density and velocity changes are interrelated and must be consistent. If the density changes cannot be modelled consistently with corresponding velocity changes, they are presumably caused by non-equilibrium. Another cause for density changes without corresponding velocity changes is due to observational selection function. Our preliminary testings show that confusing these two reasons in modelling is possible and can cause biased results.

6 CONCLUSIONS

An application to the SN we came to the following conclusions.

(i) The developed method gives consistent results for the radial acceleration ($-6360 \text{ km}^2 \text{ s}^{-2} \text{ kpc}^{-1}$, corresponding to circular

velocity 228 km s^{-1} ; see Table 2) compared to previous circular velocity estimates 238 km s^{-1} (Schönrich 2012). While other studies have used data spread over large regions, we estimated the same quantity based on the data within 0.5 kpc , assuming solar velocity from Malhan et al. (2020).

(ii) When looking at the angular momentum distribution of the non-stationarity function $h(L_z)$, we see that all perturbed stars are populating faster (presumably thin disc) orbits.

(iii) When studying the angular momentum L_z of the perturbed stars we found them to be near $L_z \approx 2100 \text{ km s}^{-1} \text{ kpc}$. As this is larger than the angular momentum corresponding to the circular speed of SN ($\approx 1900 \text{ km s}^{-1} \text{ kpc}$), hence they must be nearer to their pericentre than compared to their circular speed. We propose that their origin is from larger radii. An alternative is that the stars that rotate faster are sensitive to comoving perturbations by a component that rotates faster than the stellar disc. This source of acceleration is presumably inhomogeneities of gas disc.

(iv) Compared to Kipper et al. (2020) we updated the local tangential acceleration estimate to include non-equilibrium. The tangential acceleration estimate is $-245 \text{ km}^2 \text{ s}^{-2} \text{ kpc}^{-1}$ (see Table 2), which would indicate the updated bar mass estimate is $1.3 \times 10^{10} M_\odot$.

In the case of precision modelling of the disc of MW with future *Gaia* DR3+ data, we can describe the major source of non-stationarity nearby. In the case of modifying equation (23) to a sum of perturbations, we can cover most sources of non-stationarity.

As for future applications, the orbital arc method provides an invaluable addition to contemporary halo studies, where interactions are searched in action space. The action space has the sensitivity to mergers smoothed out long ago, while detection of non-stationarities provides information on freshly happening events. By the freshly happening influences, we mean the non-stationarities produced by substructure: perhaps there is a dark matter subhalo, which produces dynamical friction and the wake alongside it. The wake by itself is a non-stationarity (not bound system) hence detectable at shorter time-scales. Applying this methodology in the MW halo opens new and exciting opportunities to search for. There are also already more known areas that localized acceleration field could shed light on, such as the mass of Magellanic Clouds could be determined by precision acceleration field, or exact shape of MW dark matter halo in case the observations with an excellent data quality are made of outer halo.

ACKNOWLEDGEMENTS

We thank the referee for their thorough work on the paper and comments. This work was supported by institutional research funding PUTJD907, and PRG1006 of the Estonian Ministry of Education and Research. RK thanks FINCA and Turku University for hosting him for the post-doc studies. We acknowledge the support by the Centre of Excellence ‘The Dark Side of the Universe’ (TK133) financed by the European Union through the European Regional Development Fund. This work has made use of data from the European Space Agency (ESA) mission *Gaia* (<https://www.cosmos.esa.int/gaia>), processed by the *Gaia* Data Processing and Analysis Consortium (DPAC, <https://www.cosmos.esa.int/web/gaia/dpac/consortium>). Funding for the DPAC has been provided by national institutions, in particular the institutions participating in the *Gaia* Multilateral Agreement.

DATA AVAILABILITY

The data are freely acquired from *Gaia* DR2 web page, and STARHORSE project page (Anders et al. 2019). The code used for the

analysis and posterior distribution of the modelling can be acquired by contacting the corresponding author of the paper.

REFERENCES

- Abadi M. G., Navarro J. F., Steinmetz M., Eke V. R., 2003, *ApJ*, 597, 21
- Anders F. et al., 2019, *A&A*, 628, A94
- Antoja T. et al., 2018, *Nature*, 561, 360
- Banik N., Widrow L. M., Dodelson S., 2017, *MNRAS*, 464, 3775
- Bennett M., Bovy J., 2018, *MNRAS*, 482, 1417
- Bird J. C., Kazantzidis S., Weinberg D. H., 2012, *MNRAS*, 420, 913
- Cappellari M. et al., 2013, *MNRAS*, 432, 1709
- Carlberg R. G., 2019, *ApJ*, 885, 17
- Carlin J. L. et al., 2013, *ApJ*, 777, L5
- de Lorenzi F., Debattista V. P., Gerhard O., Sambhus N., 2007, *MNRAS*, 376, 71
- Feroz F., Hobson M. P., 2008, *MNRAS*, 384, 449
- Feroz F., Hobson M. P., Bridges M., 2009, *MNRAS*, 398, 1601
- Feroz F., Hobson M. P., Cameron E., Pettitt A. N., 2019, *Open J. Astrophys.*, 2, 10
- Gaia Collaboration, 2016, *A&A*, 595, A1
- Gaia Collaboration, 2018, *A&A*, 616, A1
- Garbari S., Read J. I., Lake G., 2011, *MNRAS*, 416, 2318
- Haines T., D’Onghia E., Famaey B., Laporte C., Hernquist L., 2019, *ApJ*, 879, L15
- Han J., Wang W., Cole S., Frenk C. S., 2016, *MNRAS*, 456, 1003
- Helmi A., Babusiaux C., Koppelman H. H., Massari D., Veljanoski J., Brown A. G. A., 2018, *Nature*, 563, 85
- Hilmi T. et al., 2020, *MNRAS*, 497, 933
- Johnston K. V., Bullock J. S., Sharma S., Font A., Robertson B. E., Leitner S. N., 2008, *ApJ*, 689, 936
- Jung C., Zotos E. E., 2015, *Publ. Astron. Soc. Aust.*, 32, e042
- Katz D. et al., 2019, *A&A*, 622, A205
- Kawata D., Baba J., Ciucă I., Cropper M., Grand R. J. J., Hunt J. A. S., Seabroke G., 2018, *MNRAS*, 479, L108
- Kipper R., Tempel E., Tenjes P., 2019, *MNRAS*, 482, 1724
- Kipper R., Tenjes P., Tuvikene T., Ganeshiaiah Veena P., Tempel E., 2020, *MNRAS*, 494, 3358
- Kipper R., Tamm A., Tempel E., de Propriis R., Ganeshiaiah Veena P., 2021, *A&A*, 647, A32
- Leung G. Y. C. et al., 2018, *MNRAS*, 477, 254
- Long R. J., Mao S., 2010, *MNRAS*, 405, 301
- Malhan K., Ibata R. A., Martin N. F., 2020, preprint ([arXiv:2012.05271](https://arxiv.org/abs/2012.05271))
- Moster B. P., Macciò A. V., Somerville R. S., Johansson P. H., Naab T., 2010, *MNRAS*, 403, 1009
- Ramos P., Antoja T., Figueras F., 2018, *A&A*, 619, A72
- Rix H.-W., Bovy J., 2013, *A&AR*, 21, 61
- Salomon J.-B., Bienaymé O., Reylé C., Robin A. C., Famaey B., 2020, *A&A*, 643, A75
- Schönrich R., 2012, *MNRAS*, 427, 274
- Syer D., Tremaine S., 1996, *MNRAS*, 282, 223
- Tremaine S., Weinberg M. D., 1984, *ApJ*, 282, L5
- Trick W. H., Coronado J., Rix H.-W., 2019, *MNRAS*, 484, 3291
- Vasiliev E., Belokurov V., Erkal D., 2021, *MNRAS*, 501, 2279
- Villalobos Á., Helmi A., 2008, *MNRAS*, 391, 1806
- Wegg C., Gerhard O., Portail M., 2015, *MNRAS*, 450, 4050
- Widmark A., Laporte C., de Salas P. F., Monari G., 2021, preprint ([arXiv:2105.14030](https://arxiv.org/abs/2105.14030))
- Widrow L. M., Gardner S., Yanny B., Dodelson S., Chen H.-Y., 2012, *ApJ*, 750, L41
- Williams M. E. K. et al., 2013, *MNRAS*, 436, 101
- Wozniak H., 2020, *A&A*, 642, A207
- Yanny B., Gardner S., 2013, *ApJ*, 777, 91
- Zhu L. et al., 2014, *ApJ*, 792, 59
- Zhu L., van de Ven G., Méndez-Abreu J., Obreja A., 2018, *MNRAS*, 479, 945

This paper has been typeset from a $\text{\TeX}/\text{\LaTeX}$ file prepared by the author.